

## Modeling Evaporation, Shrinkage and Cracking of Desiccating Soils

L.B. Hu, T. Hueckel

*Dept. of Civil and Environmental Engineering, Duke University, Durham, North Carolina, USA*

H. Péron, L. Laloui

*Soil Mechanics Laboratory, Ecole Polytechnique Fédérale de Lausanne (EPFL), Lausanne, Switzerland*

**Keywords: desiccation, shrinkage, soils, evaporation**

**ABSTRACT:** Room temperature drying tests on silt slurry with free and constrained boundaries, reveal an initial phase with a significant shrinkage at full saturation. Hence, this shrinkage is linked to a mass loss of pore fluid through the external boundary. Shrinkage in the unsaturated phase is much smaller. A simultaneous porosimetry reveals a bi-modal pore size distribution with a distinct evolution. In a microscopic model a bundle of deformable capillary vessels represent the modal size pores. Larger mode pores dominate the deformation, the smaller ones contributing little. A transition to an unsaturated phase occurs when the negative pore fluid pressure at the vessel exit reaches the pressure of fluid cavitation in large, then small vessels. Further desaturation is a result mainly from migration of the evaporation interfaces. Cracking arises due to an excess of radial tensile stress due to a constrained kinematics, which is three times higher than during free drying.

### 1 Introduction

Recent room temperature desiccation experiments (Peron et al. 2006) on soils initially saturated near liquid limit indicate that most of the shrinkage occurs during the saturated phase of the drying process, as opposed to the subsequent unsaturated phase. This is in agreement with a general perception that unsaturated soil has a much higher stiffness than saturated soil. This appears to be quite a universal behavior (Kodikara et al. 1999) and independent of the type of soil and type of pore fluid, as shown recently by Hu et al. 2007, who examined two different silts with three different pore fluids. (see Fig. 1). That includes shrinkage of soil permeated with ethanol solution, which has surface tension coefficient that is less than a half of that of water.

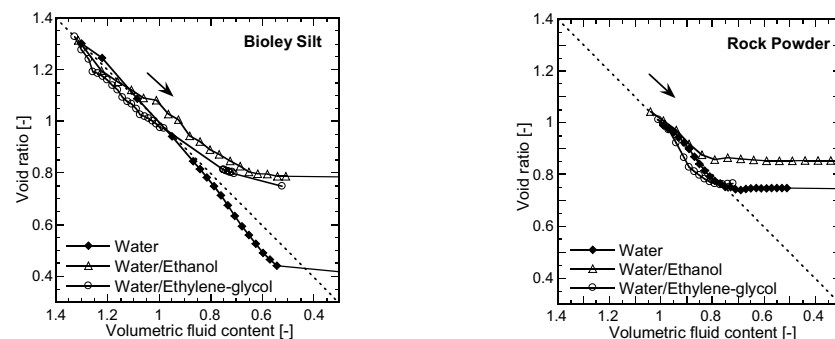


Figure 1. Void ratio evolution during drying versus the volumetric fluid content change in clayey silt [Bioley silt] (left) and a granite powder (right) filled with water, water/ethanol 50%-50% mixture and water-ethylene glycol 65%-35% mixture (see Peron et al. 2007 for details).

When soil becomes unsaturated, shrinkage practically stops, while the water content is still above 20%. Hu et al. 2007 have also shown that the amount of deformation during the saturated drying and the shrinkage limit in terms of void ratio depend on the deformability of the solid, but seems to be independent of surface tension and/or fluid saturation vapor pressure, and fluid viscosity. However, the rate of fluid loss and rate of shrinking are dependent on the evaporative and hydraulic conductivity properties, that is those of the fluid. As it is generally agreed that capillary effects are caused by the fluid surface tension, it is concluded that the saturated phase of drying is largely independent from capillary effects. Hence, shrinkage is due to the fluid removal from the pore space via Darcian flow, while fluid-gas interface is confined to the external soil mass boundary, where all the phase

transition takes place. Furthermore, it follows that the so-called “skin effect” is a negligible factor in deformation. A microscopic model of pore system deformation and transport is proposed to corroborate this hypothesis in relationship to the actual data on the evolution of the pore space. A macroscopic counterpart model has been recently developed using Biot and Darcy theories by Hu et al. 2007.

## 2 Pore space evolution

Pore size distribution was obtained for Bioley clayey silt filled with water using Mercury Intrusion Porosimetry (MIP). The measurements were conducted at the value of the water content of 33.1%, 24.8% and at 0.8%. These instants correspond to the initial state, near the shrinkage limit, and after the completion of the drying, Fig. 2. It is noted that: (1) the initial pore size is visibly bi-modal, with Large Pores (LP), defined as between  $0.6\mu\text{m}$  and  $3\mu\text{m}$  occupying initially 17% of the volume of the medium, and Small Pores (SP), defined as between  $0.09\mu\text{m}$  and  $0.6\mu\text{m}$  occupying initially 21% of the volume of the medium (see Peron, 2008 for details). (2) near shrinkage limit, the LPs take less than 5% of the volume of the medium, whereas the volume of SPs amounts to 29%. Finally, near the completion of drying, the LPs take less than 0.5% of the volume of the medium, whereas the volume of SPs remains almost unchanged, amounting to 27%.

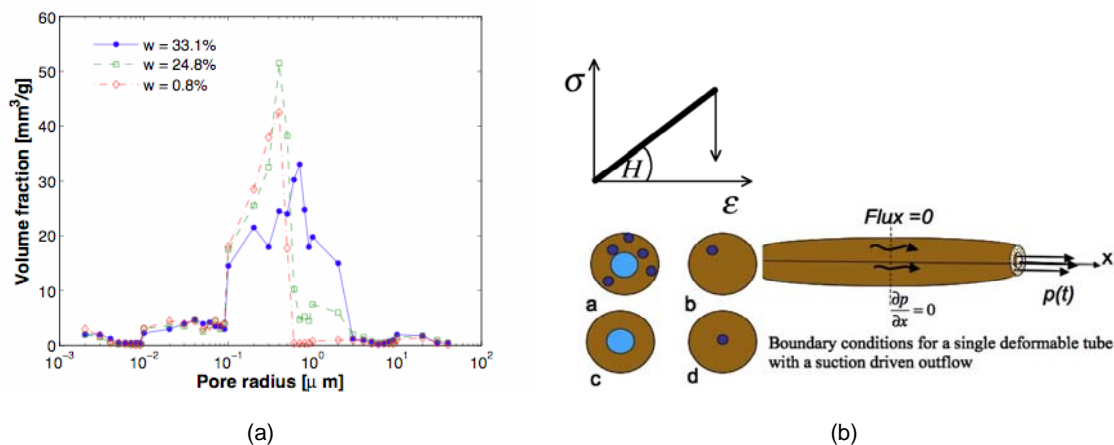


Figure 2. (a) Pore size distribution evolution during shrinkage due to isothermal drying of Bioley silt. (b) Schematics of a pore system in a cylindrical REV [a] and a BVP for a Small [b] eventually approximated via [d] and for a Large Pore via [c]. Inset: stress–strain law adopted in simulation

The porosimetry evolution indicates that during the entire process the SPs do not decrease significantly, neither in size nor in total volume they occupy. To the contrary, at near shrinkage limit, their volume somewhat increases. They probably include the volume of former LPs. The LP sizes nearly disappear at the end of drying, partially becoming SPs. Similar results were obtained by Cuisinier and Laloui (2004) and Koliji et al. (2006). It has been known for sometime that in bi-modal porosity soils, the SPs remain virtually unchanged during consolidation, whereas all volume changes are accommodated by LP changes (Delage and Lefebvre 1984). During desiccation such evolution of the pores implies that in the saturated phase most of the water evacuated comes from LPs, and hence most of the shrinkage is produced by the volume loss of that water.

## 3 Microscopic model of pore space evolution

### 3.1 Formulation

The pore system of soil is idealized as a bundle of straight tube pores of two initial sizes: small (SP) and large (LP), with their internal diameters coinciding with the average values of the pore modes, identified as  $0.5\mu\text{m}$  and  $1.5\mu\text{m}$ . The total initial volumes of the pores are set as equal to the initial value of the pore space of the corresponding modal volumes. The external radii of the tubes assumed as  $3.6\mu\text{m}$  are calculated to match the total volume of the solids of all the tubes and the total volume of the solids.

A representative elementary volume (REV) is a deformable single cylindrical thick-walled vessel around a single cylindrical LP located centrally and a series of parallel cylindrical Small Pores, as shown in Fig. 2b ([a]). The macroscopic experiments (see Peron et al. 2006) indicate that drying shrinkage strain is largely irreversible, while in the unsaturated phase the deformation is reversible to the state of the onset of desaturation, upon the removal

of suction or re-wetting. Hence, the solid of the tube is a deformable porous material, assumed as rigid-plastic. Specifically, a linear stress-strain law will be adopted for the loading phase while unloading is considered as perfectly rigid (inset in Fig. 2b). This allows us to use the principle of superposition and hence represent the pore system of Fig. 2b ([a]) as a superposition of effects of a LP and multiple SPs. Eventually for the reasons of simplicity, SP will all be located centrally as well. Hence computationally, the problem is reduced to that of a single tube with a single cylindrical pore.

The tube is considered as symmetric, axially and with respect to its central mid-plane, initially filled entirely with water, exchanging gas and fluid at their extremities with the atmosphere. Water undergoes a viscous (Poiseuille) uniaxial flow. For the external boundary conditions for the fluid one can envision either a known (negative) water pressure history, resulting from the evaporation flux. The removal of water from the tube implies that its volume is compensated by the deformation of the tube. The time evolution of the fluid negative pressure [reconstructed from the experiment (Peron et al. 2005, 2006)], is nearly linear (constant flux). At the tube mid-length no-flow condition is imposed. Viscous, non-frictional (Poiseuille) flow with an externally applied negative pressure, and is evaporation-driven.

$$\frac{\partial p}{\partial x} = -\frac{8\mu}{\pi a^4} \dot{Q} = -\frac{8\mu}{a^2} F \quad (1)$$

$\dot{Q}$  is the volume-flow rate,  $F$  is the volume flux,  $p$  is water pressure,  $\mu$  is viscosity and  $a$  is the inner radius of the tube. We assume that the flow is solely attributed to the loss of volume of the inner conduit, i.e. due to the change in  $a$ , thus the volume change of the cavity of an infinitesimal tube element per the original volume of REV per unit time is

$$\frac{\partial v}{\partial t} = \frac{2\pi a}{\pi a^2} \frac{\partial a}{\partial t} = \frac{2}{a} \frac{\partial a}{\partial t} \quad (2)$$

The mass balance requires (in 1D) that  $\partial v / \partial t = -\partial F / \partial x$ . Thus substituting the flux eq. (1), an approximate Poiseuille's equation for the collapsing tube is obtained

$$\frac{16\mu}{a^3} \frac{\partial a}{\partial t} = \frac{\partial^2 p}{\partial x^2} + \frac{2}{a} \frac{\partial a}{\partial x} \frac{\partial p}{\partial x} \quad (3)$$

Because of the linear strain-stress law adopted, the tube radius  $a$  can be expressed as a function of pressure. We adopt a simplification of Fung (1984) (valid in large strain range) who expresses the change in radius as a function of the inner pressure by ignoring the radial strain,

$$a(x) = a_0 \left[ 1 - \frac{a_0 p(x)}{Hh} \right]^{-1} \quad (4)$$

$H$  is the stiffness modulus,  $a_0$  is the initial value of the inner radius  $a$ ,  $h$  is the thickness of the tube. Fung has shown that the above approximation is very good, especially for low values of Poisson coefficient. Substituting (4) into the original eq. (3) produces a partial differential equation for pore pressure  $p$ .

$$\frac{\partial^2 p}{\partial x^2} + \frac{2a_0}{Hh \left[ 1 - \frac{pa_0}{Hh} \right]} \left( \frac{\partial p}{\partial x} \right)^2 = \frac{16\mu}{a_0} \frac{\left[ 1 - \frac{pa_0}{Hh} \right]}{Hh} \frac{\partial p}{\partial t} \quad (5)$$

The initial condition is: at  $t=0$ ,  $p=p_0=0$ . The boundary conditions are as follows:  $x=0$ ,  $\partial p / \partial x = 0$  and  $x = \pm L$ ,  $p=p(t)$ . Eq. (5) is a parabolic PDE. Its solution has been obtained using Mathlab®.

Notably, in the saturation phase the surface tension occurs at the fluid/gas interface at the tube ends only. Its role in generating axial strain and radial displacements was numerically assessed and found to be by far marginal (see Hu, 2008 for details).

### 3.2 Simulations of the saturation phase of the process

Simulations were performed separately for large and small pores. The numerical value of the stiffness modulus  $H = 125$  kPa, and of water viscosity are chosen the same for the analyses of the LP and the SPs. The length of both tubes is 30 cm (hence  $L=15$ m), taken as the length of the macroscopic experiment sample (see Peron et al. 2005). Both types of pores are subjected to the same external negative pressure evolution, as resulting from the same flux of water vapor (see Hu et al. 2007). The most significant difference between the behavior of the two types of pores is in the characteristics of closure of the inner cavity: in 10 hours needed for reaching the cavitation pressure, the SP radius closes over  $0.08 \mu\text{m}$  at the internal boundary with the original value of  $0.5 \mu\text{m}$ , whereas the LP radius closure amounts to  $0.72 \mu\text{m}$  of the original  $1.5 \mu\text{m}$ . The profiles of the opening along the axis for each pore type are shown in Fig. 3b. The resulting cumulative volume loss via single LP and 12 SPs is shown in the saturated phase of Fig. 6 in the subsequent section. The detailed results for this simulation are provided in Hu et al. 2008.

On the mechanics side of the problem it is interesting to note that because of the common value of the externally

applied negative pressure for both types of tubes throughout almost the entire history of the drying process in the saturated range their pressures are very similar. It has to be realized however, that the two types of tubes have drastically different stiffness because of the differences in their wall-thickness. This indeed produces such a dramatically different response in terms of the deformation of the tubes.

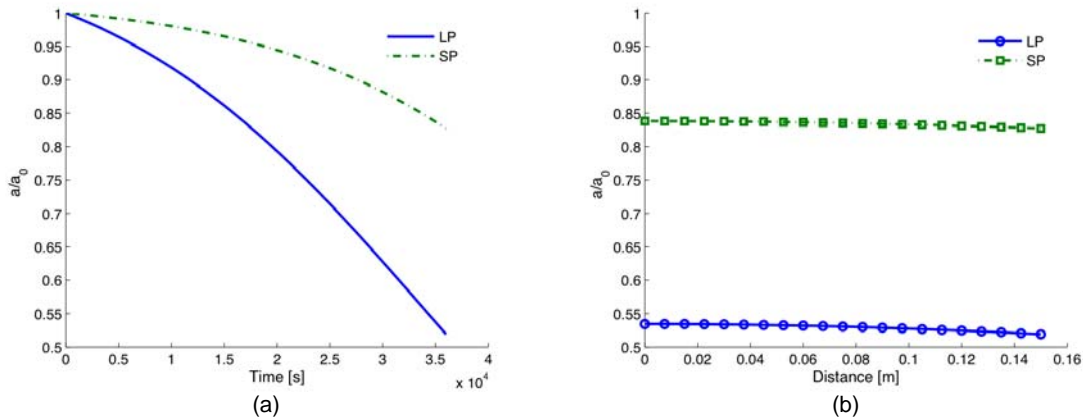


Figure 3. (a) Evolution of radii in LP and SP at  $x=L$ . (b) Profiles of radii in LP and SP after 10 hours of drying.

## 4 Post-saturation phase

### 4.1 Mechanisms of desaturation in terms of cavitation or air entry

All the precedent considerations are strictly limited to the phase in which the tube is fully saturated with water, with the vapor-water exchange occurring only at the end boundary ( $x=L$ ). Eventually air does enter into the pore space of the tube. Macroscopically, the value of suction (difference between air pressure and water pressure) at the onset of desaturation is usually referred to as the air entry value, suggesting that the water negative pressure plays a critical role in determining when gas phase intrudes an initially saturated porous body. The microscopic interpretation refers commonly to the Laplace law that describes stability of an air-fluid-solid interface, defined through an equilibrium capillary pressure,  $p_c^*$ , which depends on the interface curvature radius  $r$ , surface tension  $T_s$  and contact angle  $\theta$ .

$$p_c^* = \frac{2T_s \cos \theta}{r} \quad (6)$$

When the capillary pressure  $p_c$  rises above that value  $p_c > p_c^*$ , the equilibrium of the interface is upset and a breakthrough of air entry is considered to take place.

A clear theoretical definition of air entry value remains elusive and is factually determined empirically as a macro-scale material property. Fredlund and Rahardjo (1993) suggest that eq. (6) gives the air entry value with curvature radius being the maximum pore radius. Despite the complexity of the actual pore size distributions, such a simple formula amazingly provides a satisfactory prediction for air entry value macroscopically.

Alternatively, one can view the air intrusion as an under-surface cavitation occurring in the liquid water when at a constant temperature water is brought to evaporation condition through the evolution of the (negative) pressure, similarly to Or and Tuller, 2002. Gawin et al., 1998 postulated that cavitation arises due to suction increase in soil water at a site of a dilatant strain localization, as observed experimentally by Mokni and Desrues (1998).

### 4.2 A sharp interface evolution during desaturation

Following the criterion for cavitation as a condition for isothermal evaporation, it is postulated that once the pressure in water at a point in the vessel drops so that the capillary pressure is below the equilibrium value, eq. (6), an interface forms within the tube between liquid phase and gas phase. In the saturated phase it may be seen that the evolution of pore pressure favors such a condition at the vessel extremity, where the pressure has a minimum. Notably, such an evolution implies that at a time increment  $\delta t$  after the pressure attains the cavitation value  $p = -p_c^*$  at the vessel exit ( $x=L$ ), the interface moves incrementally inward the vessel.

The subsequent process including an inter-phase transfer of liquid water and water vapor could develop following several scenarios. For instance, in a macroscopic simulation Mainguy et al. 2001 assume that a water-vapor-dry air mixture, the exchange mass takes continuously at every point within the REV. In our experiments (which all initiated at full saturation) it has been observed that a sharp interphase interface forms, especially marked when

the evaporation rate is very high. Therefore, in the present microscopic vessel model, only the case of a sharp interface is considered that separates a fully saturated liquid water phase and an entirely gaseous phase consisting of water vapor and dry air and which progresses toward the center of the vessel in the axial direction. Extending the simulation from the preceding sections, we model the partially saturated phase of the process by simulating the onset of cavitation at the interface, at  $x=s(t)$ , imposing the condition that the negative pore pressure reaches and maintains a critical (negative) value (cavitation)  $p_{crit}$  determined by Laplace law eq. (6).

$$x = s(t): p = p_{crit} \quad (7)$$

In general, this value depends on the variable pore radius. Hence, the formulation is a generalization of Stefan problem in which the mass conservation (eq. (3)) only holds for the domain  $0 \leq x \leq s(t)$ . The kinetics of this interface position  $s(t)$  is governed by the phase transition,

$$\rho_w \frac{ds}{dt} = \lambda \frac{\partial p}{\partial x} - \xi \frac{\partial c}{\partial x} \quad (8)$$

The left hand side is the rate of mass exchange per unit area due to interface movement, the first term of the right hand side represents the water mass flux, as  $\lambda$  is the Poisseuille constant, the second term of the right hand side represents the vapor flux coming out of the interface and entering the gas phase, as  $c$  is mass concentration and  $\xi$  is the diffusion coefficient of the vapor.

It is furthermore assumed that gas pressure in the gas filled part of the vessel equals to atmospheric pressure, while the deformation of the vessel remains constant at the value developed during the saturated part of the process, as stress in this part of the vessel remains in the rigid domain. The water filled part of the vessel is described by the same equations as in the previous sections.

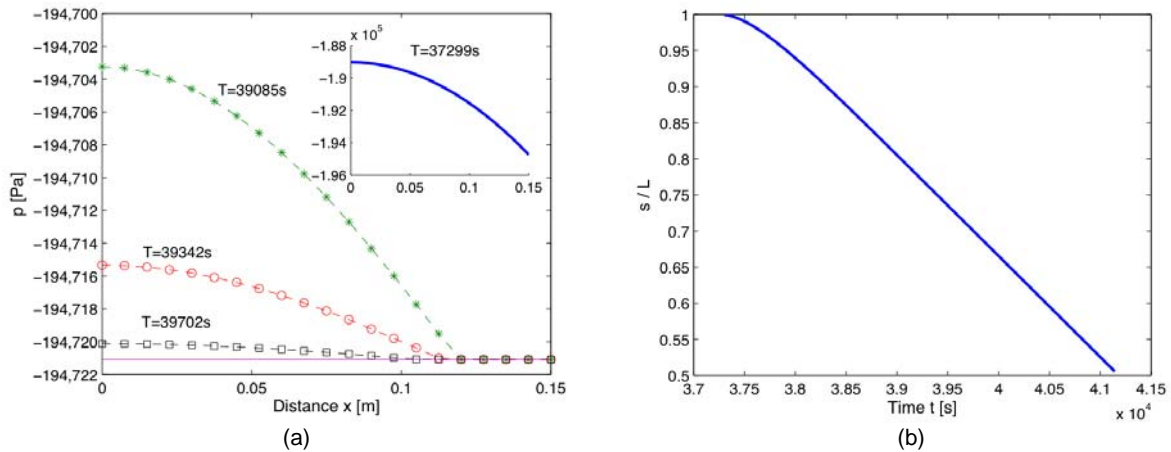


Figure 4.a) Evolution of the pressure profile during complete saturated and unsaturated tube phases (Inset: the pressure distribution at the onset of desaturation,  $T=37299s$ ). b) Motion of the interface along the tube axis.

The problem is solved in a finite difference scheme (Crank, 1984) coded in Matlab<sup>®</sup>. We further simplify the computation by taking the critical cavitation pressure value as radius independent, as the gaseous part of the vessel is assumed to be in the rigid state. Figure 4a shows the evolution of the water pressure distribution for a LP along the tube axis during both saturation phase and partial saturation phase. Figure 4b presents the evolution of the interface location. From Figure 4a and b, it can be seen that when the water pressure reaches the value of  $p_{crit}$ , the interface starts to migrate from the end boundary toward the center of the tube. Meanwhile, the (negative) water pressure in the (saturated) tube part continues to evolve, decreasing further until it reaches the value of critical (cavitation) pressure, which is hypothesized as a constant in this particular simulation. This process is very fast, and in the performed simulation occurs within 42 minutes. After that the pressure gradient is nearly zero. Consequently, the flow of fluid ceases, as does the deformation process. The water removal proceeds exclusively through evaporation across the interface, which moves also relatively fast (slightly more than 2 1/2 hour in the simulation). After the interface reaches the mid-section of the tube, the tube is considered as empty of fluid. Naturally, an assumption of a varying critical cavitation pressure dependent on the evolving pore size could lead to a more accurate simulation. However, the presented results entail, in good accordance with the macroscopic experimental observation, that immediately after air entry, the suction varies little during a long range of continuous drying.

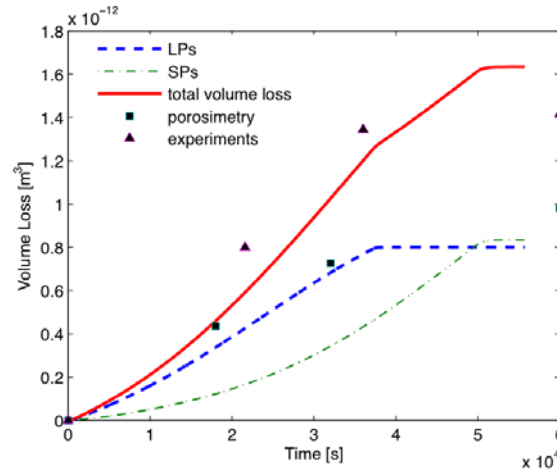


Figure 5. The pore volume loss in a REV (Fig. 2b) for LPs (dash line); SPs (dot dash line); LPs+SPs (solid line); result calibrated from the MIP study (square); result calibrated from experiments in Peron et al. 2006 (triangle).

Both large and small tubes start the saturated drying phase at the same time. While the small tubes individually produce a smaller flux, their total flux is about half of that effected by the single large tube. The difference in the pore size between LP and SP also uniquely determines the cavitation pressure value at which the two tube types enter the unsaturated tube phase. Figure 5 presents the contribution of the LP and the whole population of SP, together with the cumulative effects in terms of the total pore volume loss. Note, that the plateau for each and cumulative pore population means the end of the pore fluid pressure driven deformation process, while subsequent phase consisting of the interphase interface motion does not imply any further deformation.

Clearly, this is an idealized picture, in which only two distinct pore modes represent the entire population. The proposed analysis can be extended for the actual or a statistical representation of pores.

Also, the post-saturation scenario adopted implies that the entire cross section of a tube is free of fluid phase. An alternative scenario, with a more articulated distribution of vapor and fluid, including a distributed evaporating surface area within a non-saturated portion of the tube is presented by Hu (2008).

## 5 Microscopic simulation of a constrained porous body

Damage of soils during desiccation is considered as a response of soil to an excess of tensile stresses induced by the shrinking body with a constrained kinematics (Peron et al. 2006, Hu et al. 2006). Hence, it is of great interest to extend the presented microscopic pore model to examine a capillary vessel, with a fixed external boundary that does not allow any radial displacement at the outer radius  $r=b_0$ . All the elements of the simulation in Section 3 are still valid, except that the relationship between the inner pressure and the inner displacement (the inner radius does change) must be recalculated according to the solution for the tube with a new boundary condition: at  $r=b_0$ ,  $u=0$ .

Hence a counterpart of eq. (4) is established based on the solution to this new BVP (following Fung, 1984, the shear effect is neglected),

$$a(x) = \frac{p}{E} \frac{ha_0^2}{(a_0^2 + b_0^2)} + a_0 \quad (9)$$

It should be pointed out that the above expression is an approximate one, similar to Fung's (eq. (4)), Hence, to facilitate the comparison between a free shrinking tube and an externally constrained tube, we furthermore dramatically simplify the transport and mass conservation equation by neglecting the effect of changing radii on the Poiseuille flow movement, and the effect on the mass flow calculation due to the cross-section area change. A simple partial differential equation is obtained for the externally fixed tube

$$\frac{\partial p}{\partial t} = \frac{Ea_0(a_0^2 + b_0^2)}{16\mu h} \frac{\partial^2 p}{\partial x^2} \quad (10)$$

For the sake of further comparison, the original eq. (3) for free shrinking tube is also simplified by introducing the same assumptions and presented as

$$\frac{\partial p}{\partial t} = \kappa \frac{\partial^2 p}{\partial x^2} \quad (11)$$

Clearly, the coefficients on the right hand side of the above equation, for simplicity called  $\kappa = Eha_d/16\mu$  play the role analogous to permeability at the macro-scale. The same initial condition of constant pressure as in Section 3 is applied. The boundary conditions used in this formulation are as follows:  $x=0, \partial p/\partial x=0$  and  $x=\pm L, \kappa \partial p/\partial x = f_{evp}$ . The boundary flux at the end boundary is prescribed as an evaporation flux, taken as constant.

Figure 6a shows the water pressure evolution for these the unconstrained and constrained large pore tubes at the end boundary. Clearly, although the water volume losses are identical, as prescribed by the boundary flux condition, almost a three times higher value for water pressure is obtained for the constrained tube. Figure 6b shows the radial and circumferential stresses for these two tubes. It is evident that the tensile stress component (negative in Figure 6b) is much larger across the constrained tube. Clearly an analogous calculation may be conducted for small pore tubes as well.

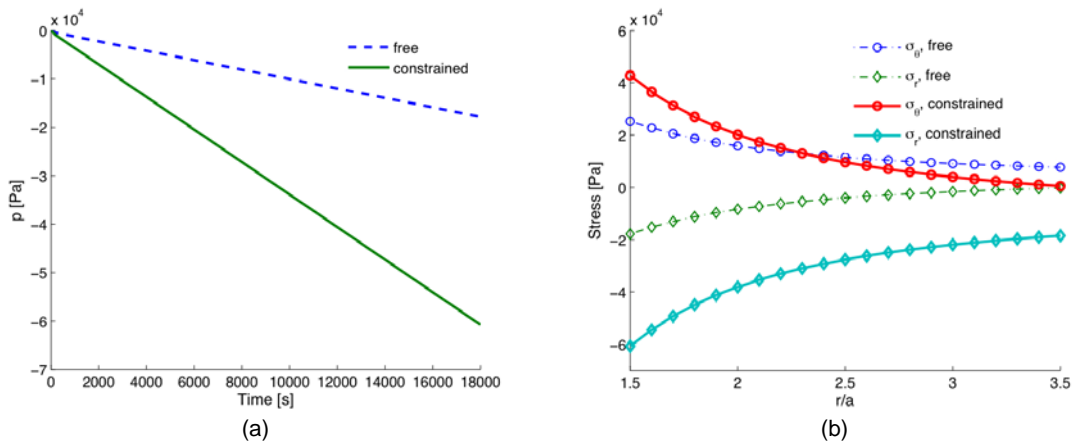


Figure 6. a) Evolution of the water pressure at  $x=L$  for the free and constrained large pore vessels. b) Stress components across the vessel wall.

## 6 Discussion and Conclusions

The presented microscopic model and numerical simulations of the drying process in its saturation phase indicate that the evolution of a highly idealized physical model reveals a series of characteristics that agree qualitatively with the experimental findings. The centerpiece of the model is transport of water toward the perimeter of the drying body producing collapse of the vessels. The model is largely based on the evolution of the pore system, idealized as bimodal. In particular, a significant reduction in diameter of large pores is seen, compared to that of smaller mode pores that is attributed to the difference in their deformability due to size difference of their wall.

The air entry mechanism is adopted to mark the onset of desaturation via cavitation understood as isothermal onset of evaporation, using a criterion of a cavitation pressure. The numerical model simulates a particular microscopic scenario with a moving phase interface inside the pore. This extends our previous simulations of the saturation phase of the drying process by incorporating the partial saturation phase of the process into the model, thus completes the framework for modeling all the phases according to a particular scenario of drying process. For this particular simulation, calibrated to the experimental findings, the saturated tube phase lasts 12 hours, whereas unsaturated tube phase lasts two and a half hours. In the presented scenario, virtually no further shrinkage is associated with this phase.

A microscopic model for a constrained pore body is examined with the resulting distinct expression for the deformation due to displacement-fixed boundary condition. As expected, the stresses generated across the tube are significantly higher, and the tensile radial stress reaches a value nearly three times higher than that in a free shrinking tube.

The presented modeling is limited to microscale mechanisms, and hence possible quantitative comparisons with experiments require careful upscaling. However, the major qualitative conclusion from the presented work is that, at least on the microscale, the drying related response driven by the negative pressure of fluid alone allows one to obtain reasonable results. The dewatered portion of the pore does not exert any pressure. Numerical comparisons with an alternative scenario that does include an explicit variable of diffused capillary forces within a partially dewatered portion of the pore space are discussed elsewhere (Hu, 2008).

Several simplifications and assumptions require further investigations, to start with the deformation modulus of the medium that comprises (only) smaller pores. An obvious emerging task is to investigate the effect of varying cavitation (or air entry) critical pressure defined in Laplace law. A microscopic criterion for this occurrence is still a point of discussion. Verification of the validity of the present model requires an up-scaling procedure to represent

the proposed mechanisms at the macroscale as well as more experiments designed to address those aspects.

## 7 Acknowledgements

This work is funded in cooperation between the Swiss National Science Foundation, grant 200020-109661 and the US National Science Foundation, grant # 0324543.

## 8 References

- Abu-Hajleh, A.N., Znidarcic D. 1995, Desiccation theory for soft cohesive soils, *J. Geotech. Eng.* **121**(6): 492 – 502
- Crank J. 1984. *Free and Moving Boundary Problems*. New York: Oxford University Press
- Cuisinier, O., Laloui, L. 2004, Fabric evolution during hydromechanical loading of a compacted silt, *Int. J. for Numerical and Analytical Methods in Geomechanics*, **28**: 483-499
- Delage, P., Lefebvre, G. 1984, Study of the structure of the sensitive Champlain Clay and of its evolution during consolidation, *Canadian Geotechnical J.*, **21**(1): 21 -35
- Fredlund, D.G., Rahardjo, H. 1993, *Soil Mechanics for Unsaturated Soils*. New York: John Wiley & Sons
- Fung, Y.C. 1984. *Biodynamics: Circulation*. New York: Springer
- Gawin, D., Sanavia, L., Schrefler, B.A. 1998. Cavitation modelling in saturated geomaterials with application to dynamic strain localization. *International Journal for Numerical Methods in Fluids*, **27**:109-125
- Hu, L.B. 2008. *Physico-chemo-mechanical Coupling Mechanisms in Soil Behavior*. Ph.D. Dissertation. Duke University. Durham, NC, USA
- Hu, L.B., Peron, H., Hueckel, T., Laloui, L. 2006. Numerical and phenomenological study of desiccation of soil. In N. Lu, L.R. Hoyos and L. Reddi (eds.), *ASCE Geotechnical Special Publication 148: Advances in Unsaturated Soil, Seepage, and Environmental Geotechnics*, 166-177
- Hu, L.B., Peron, H., Hueckel, T., Laloui, L. 2007. Drying shrinkage of deformable porous media: mechanisms induced by the fluid removal. In H.W. Olson (ed.), *ASCE Geotechnical Special Publication 157: Geo-Denver 2007, New Peaks in Geotechnics*. 10 pages, CD-ROM
- Kodikara, J., Barbour, S.L., Fredlund, D.G. 1999. Changes in clay structure and behaviour due to wetting and drying. *Proceedings of the eighth Australia New Zealand Conference on Geomechanics*, Hobart, 1: 179-185.
- Koliji, A., Laloui, L. Cuisinier, O., Vulliet, L. 2006, Suction Induced Effects on the Fabric of a Structured Soil, *Transport in Porous Media* **64**: 261 -278
- Konrad, J.M., Ayad, R. 1997. An idealized framework for the analysis of cohesive soils undergoing desiccation. *Canadian Geotechnical Journal*, **34**: 477-488
- Mainguy, M., Coussy, O., Baroghel-Bouny, V. 2001. Role of air pressure in drying of weakly permeable materials. *Journal of Engineering Mechanics, ASCE*, **127**:582-592
- Miller, C.J., Mi H., Yesiller, N. 1998. Experimental analysis of desiccation crack propagation in clay liners. *Journal of the American Water Resources Association*, **34**(3): 677-686
- Mokni, M., Desrues, J. 1998. Strain localisation measurements in undrained plane-strain biaxial tests on Hostun RF sand. *Mechanics of Cohesive Frictional Materials*, **4**: 419-441.
- Peron, H. 2008. *Desiccation cracking of soils*, Ph.D. Thesis, Ecole Polytechnique Federal de Lausanne, Lausanne, Switzerland
- Peron, H., Laloui, L., Hueckel, T. 2005. An Experimental Evidence in Desiccation Cracking in Sandy Silt, in Tarantino, Romero and Cui (eds.), *Advanced Experimental Unsaturated Soil Mechanics*, Proceeding of Conference, Trento, Italy, April 2005, Taylor and Francis Group, London, 475 – 480
- Peron, H., Laloui, L., Hueckel, T., Hu, L.B. 2006. Experimental study of desiccation of soil. In G.A. Miller, C.E. Zapata, S.L. Houston and D.G. Fredlund (eds.), *ASCE Geotechnical Special Publication 147: Unsaturated Soils 2006*, 1073-1084
- Peron, H., Hu, L.B., Hueckel, T., Laloui, L. 2007. The influence of the pore fluid on desiccation of a deformable porous material. In T. Schanz (ed.), *Springer Proceedings in Physics, Experimental Unsaturated Soil Mechanics*, 413-420